Journal of Catalysis 262 (2009) 224–234

Contents lists available at ScienceDirect

Journal of Catalysis

www.elsevier.com/locate/jcat

Insight into the properties of Fe oxide present in high concentrations on mesoporous silica

A. Gervasini [a,*], C. Messi [b], P. Carniti [b], A. Ponti [c,d], N. Ravasio [e], F. Zaccheria [e]

[a] Dipartimento di Chimica Fisica ed Elettrochimica & Centro di Eccellenza CIMAINA, Università degli Studi di Milano, via C. Golgi 19, I-20133 Milano, Italy
[b] Dipartimento di Chimica Fisica ed Elettrochimica, Università degli Studi di Milano, via C. Golgi 19, I-20133 Milano, Italy
[c] Istituto di Scienze e Tecnologie Molecolari, Consiglio Nazionale delle Ricerche (CNR-ISTM), via Golgi 19, I-20133 Milano, Italy
[d] UdR Milano Università, INSTM, via Giusti 9, I-50121 Firenze, Italy
[e] Istituto di Scienze e Tecnologie Molecolari, Consiglio Nazionale delle Ricerche (CNR-ISTM), via Golgi 19, I-20133 Milano, Italy

ARTICLE INFO

Article history:
Received 29 September 2008
Revised 17 December 2008
Accepted 18 December 2008
Available online 23 January 2009

Keywords:
Iron oxide catalysts
Mesoporous silica
Supported catalysts
Acid catalysts
Catalyst characterization
Epoxide isomerization

ABSTRACT

Oxide catalysts containing highly dispersed Fe phases supported on a mesoporous, high surface area silica, with iron in a wide range of concentration ($4 < Fe_2O_3$ mass% < 17), are presented. A suite of techniques was employed to determine the structural, morphologic, surface, electronic, acidic, and red-ox properties of the samples. Although the samples have great variation of the iron loading, they maintained good Fe-dispersion and low metal aggregation, even those with the highest concentrations of iron. By increasing the Fe-loading, the DR–UV–vis spectra showed that the band centered at 360 nm (low nuclearity 2*d*-Fe oxo entities) became more intense, while the band at 500 nm (typical of 3*d*-Fe_2O_3 nanoparticles) remained of low intensity and quite constant. Formation of significant amount of isolated Fe^{3+} centers (band at ca. 230 nm) were also identified, in agreement with EPR evidences. The titrated amount of surface acid sites increased with the Fe loading, because of the increased amount of FeO_x species, acting as Lewis acid sites. The test reaction of isomerization of α-pinene oxide revealed the prominent presence of Lewis acid sites on all the samples with main formation of the α-campholenic aldehyde product. The selectivity to α-campholenic aldehyde was around 53% for all the catalysts, independent of the Fe-loading. However, productivity to α-campholenic aldehyde increased with Fe-concentration, because of the increase of reaction rates as higher the Fe content was. Active acid Fe-sites could be associated with isolated Fe centers and in particular with low nuclearity 2*d*-Fe oxo entities.

1. Introduction

The development of solid Lewis acids is a topic of great importance in synthetic organic chemistry and it has been intensively pursued not only for a fundamental scientific interest, but also for many applications at industrial level [1,2]. Solid Lewis acids are viewed as substitutes of the more conventional homogeneous acid catalysts, metal halides (such as $ZnCl_2$, $AlCl_3$, $FeCl_3$, $SnCl_4$, and $TiCl_4$) and HF or H_2SO_4 [3–5], being able to overcome all the well-known problems of the homogeneous acids. Among the catalytic materials with Lewis acid properties proposed in the scientific literature and in patent catalysts, oxides containing dispersed metal centers represent valid candidates [6,7].

Rather large work was accomplished on the materials belonging to SiO_2–Fe_2O_3 system. In such system, high degree of coordinative unsaturation of the nanosized Fe_2O_3 clusters gives outstanding catalytic properties in exigent acid reactions, such as Friedel–Crafts alkylations reactions [8,9]. These oxide materials can be prepared with convenient porosity and nanosized iron oxide aggregates by essentially three different experimental procedures [10]. In the first one, the iron oxide phase is formed during a sol–gel process (in aqueous or organic media [11–13]) in the presence of a suitable Si-font to obtain the SiO_2–Fe_2O_3 material by one-step synthesis [14–20]. In the second method, the ion exchange capacity of the substrate matrix is exploited. In this case, facile functionalization of the surface with transition metal ions (i.e., Fe^{2+}/Fe^{3+}) can be performed. The method is particularly suitable for zeolites and related materials possessing high-ion exchange capacity [8,21,22]. In the third case, iron was introduced by post-synthesis way on a finite SiO_2 matrix. The iron oxide phase is formed by thermal treatment after impregnation, grafting, chemical deposition, adsorption of a soluble iron salt on the previously processed support matrix [23–27]. This method largely represents the conventional technique for the introduction of transition metal ions at the solid surfaces, because of the possibility to obtain high surface density of metal

* Corresponding author. Fax: +39 02 50314254.
E-mail address: antonella.gervasini@unimi.it (A. Gervasini).

0021-9517/$ – see front matter
doi:10.1016/j.jcat.2008.12.016

ions useful for high catalytic activity [28], although agglomeration of the metal centers occurred.

Bourikas et al. [29] in their review on the role of the liquid–solid interface in the preparation of supported catalysts point out the advantages of the interfacial deposition, based on the equilibration of the transition metal ionic species between the support surface and the liquid solution, in comparison with the conventional impregnation techniques (wet impregnation, pore volume impregnation, or dry impregnation). An analogous successful procedure was adopted by the group of Arena et al. [30] that presented the preparation of low-loaded iron oxide on silica catalysts by an adsorption–precipitation route. The Fe-catalysts so obtained had enhanced oxidation properties in the selective oxidation of methane to formaldehyde. Another procedure based on the adsorption-equilibrium of a metal complex dissolved in solution was recently adopted by these authors for the preparation of supported copper oxides [31,32] and iron oxide [33] catalysts. In these cases too, nanosized metal oxide phases with good homogeneous metal distribution on different supports were highlighted.

Ordered mesoporous materials (such as MCM-41/48 [34,35], SBA-15 [36], MSU-n [37], KIT-1 [38], and FSM-16 [39], among other structures) synthesized by the use of non-ionic or ionic surfactant-templating agents [40–42] have opened many new possibilities for application in catalysis [43–51], chromatographic separation [52,53], and other various fields of nanoscience [54,55] due to their tuneable pore size and very large surface area. The favorable textural properties of mesoporous silica materials make them in principle ideal materials not only for catalytic conversions of large reactant molecules that cannot diffuse into the micropores of aluminosilicate zeolites, but also as support materials [8,25].

In this work, efforts have been made to prepare isolated or oligonuclear Fe species stabilized on a mesoporous high surface area silica obtained *via* a non-calcination procedure [56], increasing the Fe-loading of the different samples up to 17 mass% of Fe_2O_3. For the catalyst preparation, particular care was devoted to the metal deposition technique that had to ensure high metal dispersion with uniform distribution of the iron centers over the silica surface. The nature of the Fe-catalytic sites still remains a moot point with various proposals stressing the importance of mononuclear, binuclear or more aggregated Fe sites for a variety of catalytic reactions [17]. Most research work appeared on low-loaded Fe-catalysts, aimed at studying the nature of the Fe-species in relation with some catalytic activity [17,24,30], while only fewer on high Fe-loaded systems. The maintenance of high Fe-dispersion in catalysts at high Fe content is not an easy task to realize and, as far as the authors know, there are no reports on amorphous Fe oxide catalysts at high Fe-loading and high Fe-dispersion.

On the prepared catalyst samples, complementary techniques including UV–vis, XPS, and EPR spectroscopies were employed to identify the electronic and coordination environment of the iron species, besides their redox properties by TPR. The surface acid properties of the catalysts were tested by both a classical titration technique (employing 2-phenylethylamine, PEA, as probe) and a test reaction sensitive to the nature of the acid sites (α-pinene oxide isomerization [57,58]), thus able to ascertain the prevalent presence of Lewis or Brönsted sites on the catalytic surfaces from the obtained product distribution. Moreover, α-pinene oxide isomerization is a reaction of some importance in the fine chemistry because one of the main products, campholenic aldehyde, is a very important intermediate used for the manufacture of sandalwood fragrances, currently being investigated together with macrocyclic musks, as possible substitutes for nitro and polycyclic musks, widespread used as fragrances in laundry detergents, fabric softeners, cleaning agents and cosmetic products, and are recognized as damaging chemical species to the environment.

2. Experimental

2.1. Sample preparation

All the products and solvents used for the sample preparation were purchased from Fluka Analytical and VWR, respectively. They are all pure (>98%) or ultra-pure (>99%) grade.

Mesoporous silica (labeled as SIM) was prepared by a modification of the procedure described by Huh et al. [56] which involves a condensation method based on sodium hydroxide-catalyzed reaction of tetraethoxysilane (TEOS) in the presence of low concentration of cetyltrimethylammonium bromide (CTAB) surfactant followed by acid extraction of the as-made-product performed in a methanol mixture of hydrochloric acid (details on the synthesis can be found in Supporting Information).

The iron phase was deposited by the previously described procedure based on an equilibrium-adsorption method [26,31–33] by using Fe(III)-acetylacetonate (Fe(acac)) as precursor of the Fe oxide phase. At first, the bare support (SIM) was suspended in a water/propanol solution (1 g in 0.012 L of 1/1 v/v solution) at the temperature of 0 °C and pH 10, maintained by ammonia solution. A water/propanol solution of Fe(III)-acetylacetonate (0.03 M), hereafter called *Solution A*, was gently dropped to the support suspension, keeping constant the pH value during addition by ammonia solution. Then, the temperature was gently left to raise up to room temperature and the system attained adsorption equilibrium during 24 h. After equilibration, a dark orange solid was recovered by filtration, dried at 120 °C overnight, and calcined at 500 °C for 4 h (Fe4/SIM, 4.10 mass% of Fe_2O_3, Table 2). For the preparation of the samples with higher concentration of Fe, *Solution A* was adsorbed on Fe4/SIM, instead of on the bare SIM, thus obtaining Fe6/SIM (6.72 mass% of Fe_2O_3). Then, *Solution A* was adsorbed on Fe6/SIM to obtain Fe12/SIM (12.90 mass% of Fe_2O_3), and it was adsorbed on Fe12/SIM to obtain Fe17/SIM (17.16 mass% of Fe_2O_3), repeating in each case all the operations of filtration, drying and calcination as above described on each sample (Scheme 1).

The iron content of the samples was determined by ICP-OES (plasma optic emission spectrometer, from Horiba JOBIN YVON) after solid dissolution in acid mixtures ($H_2SO_4 + HNO_3 + HF$) followed by evaporation and new dissolution in HNO_3.

2.2. Sample characterization

Surface area (BET) and porosity were determined by conventional N_2 adsorption/desorption at −196 °C using a Carlo Erba Sorptomatic 1900 instrument. All the sample powders were crushed and sieved between 45 and 60 mesh and then introduced in the glass-cell (ca. 0.05 g of SIM and ca. 0.2 g of the Fe-samples). Prior to the analysis, the support (SIM) was outgassed at different temperatures from 90 °C to 550 °C for 3 h, and the calcined Fe-samples were outgassed at 350 °C for 16 h. Pore volume distribution was calculated from the desorption branch of the isotherm using the Barrett–Joyner–Halenda (BJH) model equation [59].

Scanning electron micrographs (SEM) were obtained by a JEOL JSM-5500LV coupled with energy dispersive X-ray spectroscopic (EDS) analyzer working at 20 keV to obtain quantitative information on the distribution of Fe and Si elements. The samples were analyzed under moderate vacuum after gold coating.

XRD (X-ray diffraction) of the powder samples was carried out by a Philips PW1710 vertical goniometer diffractometer using Ni-filtered Cu$K_{\alpha 1}$ radiation ($\lambda = 1.54178$ Å). For ordinary measurements, the chamber rotated around the sample at 1° (2θ) min^{-1} from 3 to 80° (2θ).

UV–vis diffuse reflectance spectroscopy (UV–vis–DRS) measurements were performed on fine powders of the Fe-samples put into

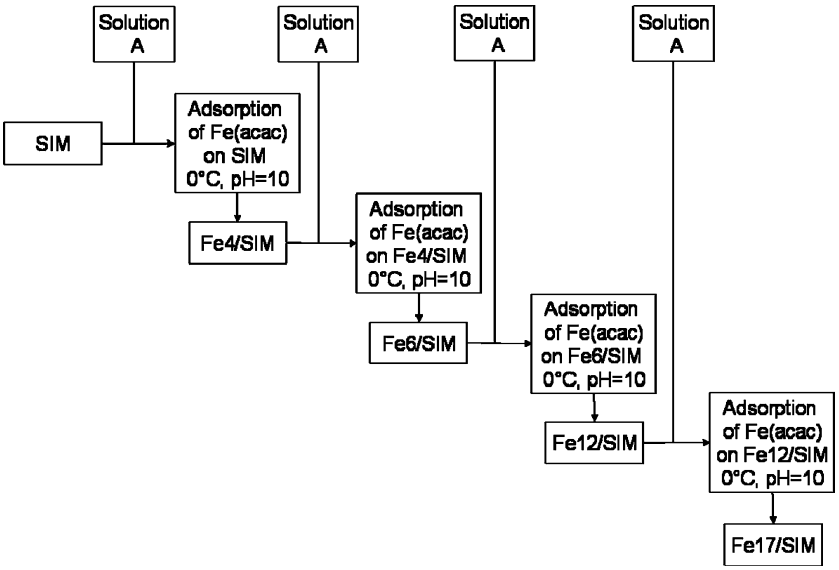

Scheme 1. Schematic representation of the procedure used for the preparation of the catalysts at increasing Fe-loading on SIM support. *Solution A* contains Fe(III)-acetylacetonate (Fe(acac)) in water/propanol solution (0.03 M).

a cell with optical quartz walls by a Perkin-Elmer Lambda 35 instrument equipped with an integrating sphere and Spectralon® as reference material. Spectra were measured in absorbance mode in the 1100–190 nm range.

Mid-infrared spectra were recorded at room temperature using a FT-IR spectrometer (Biorad FTS-40). The spectra of the powders mixed with KBr were collected in the range 4000–400 cm^{-1} by averaging 100 scans at a resolution of 4 cm^{-1}.

A TG analyzer from Perkin-Elmer (TGA7) was used for the thermal gravimetric analyses. Analyses were performed in air flowing (dried Fe-samples) or in nitrogen flowing (SIM samples) under constant rate (10 °C min^{-1}) of temperature increasing with/without intermediate isothermal plateaux. A three-step TG analysis was performed to determine the hydroxyl density on SIM surface: (i) first heating from 50° to 200 °C at a rate of 10 °C min^{-1}; (ii) then isothermal step at 200 °C for 30 min; and (iii) finally heating from 200 °C to 900 °C at rate of 10 °C min^{-1}. Before the TG analysis, the samples were stored in a vessel saturated with water at room temperature for a minimum of 16 h.

XPS (X-ray photoelectron spectroscopy) analyses were carried out by a Kratos Analytical AXIS ULTRA DLD spectrophotometer, with AlK_α monochromatized exciting radiation (1486.6 eV). Pass energy of 160 eV or 40 eV for the acquisition of the general (0–1100 eV) or high-resolution (C 1s, O 1s, Si 2p, Fe 2p) spectra was used, respectively. The residual pressure in the analysis chamber was around 10^{-9} mbar. All binding energy (BE) measurements were corrected for charging effects with reference to the C 1s peak of the adventitious carbon (284.6 eV).

The EPR (electron paramagnetic resonance) spectra were recorded by a Bruker Elexsys E560 X-band spectrometer. Typical recording conditions were: microwave frequency ca. 9.4 GHz, microwave power 5 mW (16 dB), magnetic field sweep range 800 mT (2048 points), modulation frequency 100 kHz, modulation amplitude 0.4 mT, sweep time 168 s. Spectra were taken at room temperature and at −196 °C (liquid nitrogen cold finger). Magnetic field was measured with a Bruker ER036TM teslameter; microwave frequency was measured by a Hewlett-Packard HP 5340A frequency counter.

TPR (temperature programmed reduction) experiments were performed on the Fe-samples using a TPD/R/O-1100 instrument from Thermo Electron Corporation. Sample mass used varied from 0.05 to 0.08 g (45–60 mesh particles) to obtain k and P values of 80 s and 10 °C, respectively [60,61]. The samples were initially pre-treated in air flow at 350 °C for 1 h. After cooling to 50 °C, the H_2/Ar (5.03% v/v) reducing mixture flowed through the sample whose temperature increased from 50 to 900 °C (8 °C min^{-1}). The H_2 consumption was detected by a thermal conductivity detector (TCD). Peak areas were calibrated with pure H_2 injections (Sapio, Italy; 6.0 purity) and with thermal reduction of high purity CuO wires.

The acid sites titrations were performed in cyclohexane using a HPLC apparatus working with a recirculating method, modifying a previously described method [62]. The titration of the acid sites was carried out by the 2-phenylethylamine (PEA) basic probe at 17 °C. The sample (ca. 0.050 g, 80–200 mesh particles) was first activated under air flowing (SIM at 90 °C for 3 h and the calcined Fe-samples at 350 °C for 16 h) in a stainless steel tube (i.d. 2 mm, length 12 cm). After the transfer of the tube into the adsorption line, successive injections of PEA solution (50 µl, 0.15 M in cyclohexane) were put into the line in which cyclohexane continuously circulated through the sample holder until adsorption equilibrium was achieved. The adsorption isotherms were numerically interpreted with the Langmuir model to obtain the amount of PEA adsorbed at the monolayer, µmol m^{-2}, correspondent to the amount of acid sites, µequiv m^{-2}, and the Langmuir adsorption constant (b/M^{-1}).

2.3. Catalytic reaction

The epoxide isomerization tests using α-pinene oxide (POX) as substrate were carried out at room temperature (r.t.) in batch conditions, as detailed in Ref. [58]. The catalyst sample (0.1 g) was activated into a glass reactor at 350 °C for 30 min in air and then for 30 min under reduced pressure at the same temperature. After catalyst activation, α-pinene oxide (from Fluka Analytical, 97% purity) and toluene were introduced into the reactor (0.1 g, 0.66 mmol, in 0.008 L) under N_2 atmosphere. The progress of the reaction was followed by gas-chromatographic techniques (GC from Agilent 6890 with FID detector, mounting a 5% phenyl-methylpolysiloxane column, and GC–MS from Agilent 5971 series), and proton nuclear magnetic resonance (^{1}H NMR from Bruker, 300 MHz) analysis, analyzing samples withdrawn from the reaction mixture at different times.

Table 1
Properties of the synthesized silica (SIM) used as support.

Content (mass%)		
C	0.62	
H	1.12	
N	0.06	
Structure	Amorphous	Broad band at 10–30° 2θ
Surface area ($m^2\,g^{-1}$)	883 ± 107 (12%)	
Porosity ($cm^3\,g^{-1}$)	0.90 ± 0.10 (11%)	Measured after thermal treatment (3 h) at 90, 150, 250, 350, 450, and 550 °C
Pore size (nm)	2.85 ± 0.09 (3.1%)	
Silanol density ($(OH^-)\,nm^{-2}$)	4.53 ± 0.70	
($(OH^-)\,g^{-1}$)	$(3.95 \pm 0.33) \times 10^{21}$	
IR skeletal bands[a] (cm^{-1})	3434	Si–O–H, vibration of the hydrogen bonded silanol group perturbed by adsorbed water
	1238 and 1078	Si–O–Si, asymmetric stretching vibration
	968	Si–OH, silanol vibration
	812	Si–O–Si, symmetric stretching vibration
Acidity ($\mu equiv\,m^{-2}$)	0.714	Determined by PEA titration in cyclohexane. Numerical interpretation by Langmuir model
($mequiv\,g^{-1}$)	0.618	

[a] Ref. [63].

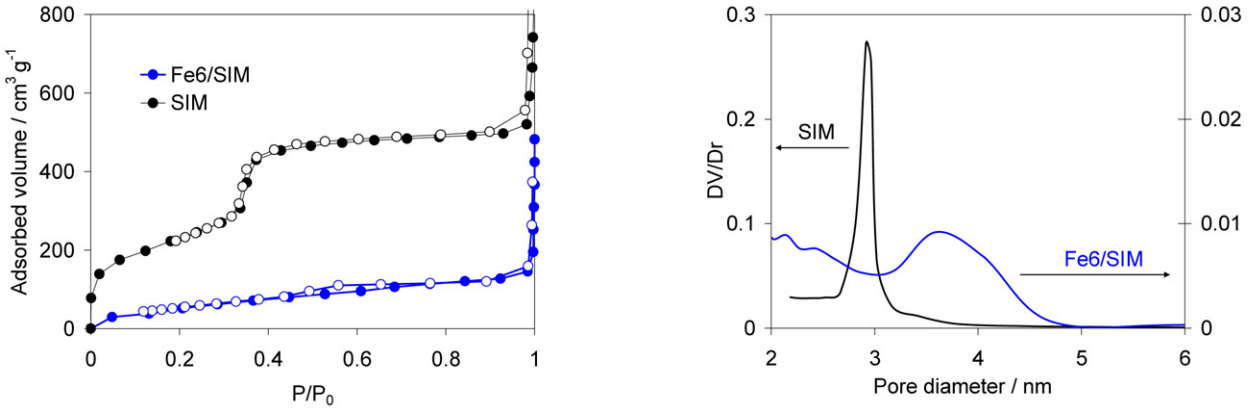

Fig. 1. N_2 adsorption/desorption isotherms (left) and BJH pore size distributions (right) of the bare silica support (SIM) and a Fe-sample (Fe6/SIM) chosen as representative catalyst.

The interpretation of the collected data confirmed that POX isomerization proceeded following a first-order kinetics to all the products that developed following a parallel reaction mechanism. The initial rate of formation of the main product (campholenic aldehyde, CPA) was calculated by the following equation:

$$r^{\circ}_{CPA} = k_{POX} \cdot S_{CPA} \cdot A_{POX}/m_{cat}, \quad (1)$$

where r°_{CPA} ($mol_{CPA}/(g_{cat}\,min)^{-1}$) is the initial rate to CPA formation, k_{POX} (min^{-1}) is the first-order kinetic constant obtained reporting $\ln(1-y)$ vs. t (with y the fractional POX conversion and t the reaction time, in min); S_{CPA} is the fractional selectivity to CPA; A_{POX} (g) is the initial amount of POX; and m_{cat} (g) is the catalyst mass.

3. Results and discussion

3.1. Sample preparation and characterization

The silica used as support matrix (SIM) was synthesized *via* a polymeric route involving the alkoxide (tetraethoxysilane) hydrolysis and condensation catalyzed by a base. The acid extraction of the collected solid, instead of the conventional calcination, completed the synthesis procedure. The FT-IR spectrum of SIM is similar to that of a conventionally prepared SiO_2, namely the bands at ca. 1078 cm^{-1} and 1238 cm^{-1}, assigned to the asymmetric Si–O–Si stretching vibrations, and the band around 800 cm^{-1}, attributing to the symmetric Si–O–Si stretching vibrations, dominate the spectrum. The other typical skeletal bands observed are reported in Table 1.

The main physical and chemical characteristics of SIM are collected in Table 1. The obtained silica sample was quite pure (very low content of C-, H-, and N-impurities) and it revealed a lack of structural order. It is known that, the structural order of the mesoporous materials depends on several parameters, such as the concentration of surfactant, synthesis temperature, hydrothermal temperature and time, total acidity, etc. all affecting the degree of hydrolysis and cross-linking of the silicates [35]. As the typical mesoporous solids, SIM showed high surface area value, of ca. 900 $m^2\,g^{-1}$, pore volume of ca. 0.90 $cm^3\,g^{-1}$, and narrow mesopore size distribution (pore diameter around 3 nm). The reversible type IV N_2-adsorption–desorption isotherms of SIM, without hysteresis loop, similar to those reported in Refs. [58,63,64], are shown in Fig. 1. The step corresponding to capillary condensation in the primary mesopores appears at relative pressure range 0.3–0.4, where a sharp inflection clearly appeared in the isotherms. The morphology and mesoporous structure of SIM did not vary after thermal treatment up to 550 °C (Table 1).

It is well known that the silica surface consists of a combination of siloxane bridges (≡Si–O–Si≡, with the oxygen on the surface) and of silanol groups (≡Si–OH, of different type) whose relative concentration depends on various factors, such as calcination temperature, ambient humidity, storage time, etc. [65]. The knowledge of the silanol surface density of the SIM surface represents an important parameter to judge on its suitability to act as support for metal oxide phases (i.e., iron phase). Following the procedure reported by Mrowiec-Bialoń [66], we used the thermogravimetric analysis to determine the silanol surface density of the SIM surface. By applying the three-step TG analysis (see Section 2)

Table 2
Properties of the Fe-catalysts.

Sample	Composition (mass%)		D_{Fe}[a]	Coverage[b]	Surface area	Porosity	Pore size[c]	Acid sites[d]
	Fe	Fe_2O_3	($atom_{Fe}\,nm^{-2}$)	(%)	($m^2\,g^{-1}$)	($cm^3\,g^{-1}$)	(nm)	($\mu equiv\,m^{-2}$)
Fe4/SIM	2.87	4.10	0.36	5.0	285	0.37	3.6	1.502
Fe6/SIM	4.70	6.72	0.59	8.6	226	0.22	3.6	1.129
Fe12/SIM	9.0	12.90	1.12	17.76	119	0.20	3.8	1.794
Fe17/SIM	12.0	17.16	1.50	24.8	102	0.16	3.7	2.154

[a] Iron surface density.
[b] Calculated support coverage by Fe_2O_3 ordered in a monolayer [70].
[c] Main pore size determined from BJH pore distribution.
[d] Determined by PEA titration in cyclohexane as solvent. Numerical interpretation by Langmuir model.

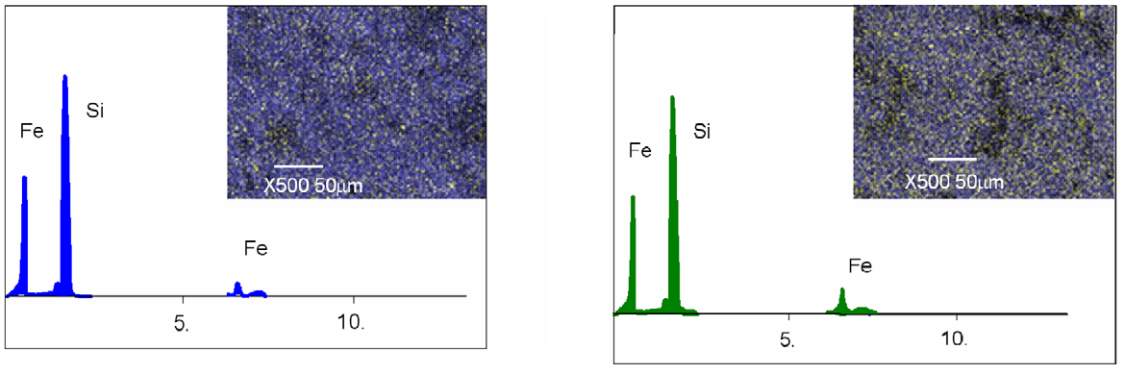

Fig. 2. EDS spectra and relevant atomic maps of Fe6/SIM (left) and Fe17/SIM (right) catalysts.

to SIM sample, we calculated the hydroxyl surface density from the mass loss observed in the 200–900 °C interval of temperature, that was due to the removal of silanol groups from the SIM surface. Any significant difference was not observed among the SIM samples thermally treated at different temperatures. The mean value calculated of 4.5 $(OH^-)\,nm^{-2}$ (Table 1) is in perfect agreement with that reported in the literature for fully hydroxylated silicas, that have 4.6 $(OH^-)\,nm^{-2}$ [67–69]. This value can be considered a constant value, independent of the silica type and structural characteristics. Because the high surface area of our silica, the silanol surface density of SIM calculated per unit mass (3.95×10^{21} $(OH^-)\,g^{-1}$) is almost three times higher than that of conventionally prepared silica samples.

The SIM coverage by the dispersed iron phase was realized by the so-called equilibrium-adsorption method from iron-acetylacetonate precursor. Because of the SIM support was not calcined, it could offer highly reactive silanol groups able to adsorb the Fe(III)-complex. Despite the amount of Fe(III) complex in suspension with bare SIM (and Fe4/SIM, Fe6/SIM, Fe12/SIM, see Scheme 1) allowed the loading of ca. 8 mass% of Fe, only a part of Fe(III) was adsorbed on the samples (Table 2). Complete decomposition of the adsorbed iron complex to form the dispersed iron oxide phase upon calcination step was confirmed by TGA analysis. The main peaks of loss of mass were located between 300 and 500 °C without any clear difference among the samples containing iron oxide at different concentration.

The iron oxide concentration of the samples was comprised in a large interval, from 4 to 17 mass% (Table 2). From the knowledge of the SIM surface area and loading amount of Fe_2O_3 on each sample, it could be calculated [70] that the portion of support surface covered by iron oxide did not exceed 25% and that the iron surface density reached the limit of 1.5 $atom_{Fe}\,nm^{-2}$ for the highest concentrated catalyst (Fe17/SIM). Atomic maps obtained from SEM-EDS analysis (Fig. 2) evidence the good distribution of iron oxide over SIM surface for two selected Fe-catalysts (Fe6/SIM and Fe17/SIM). The iron phase appears regularly distributed over the

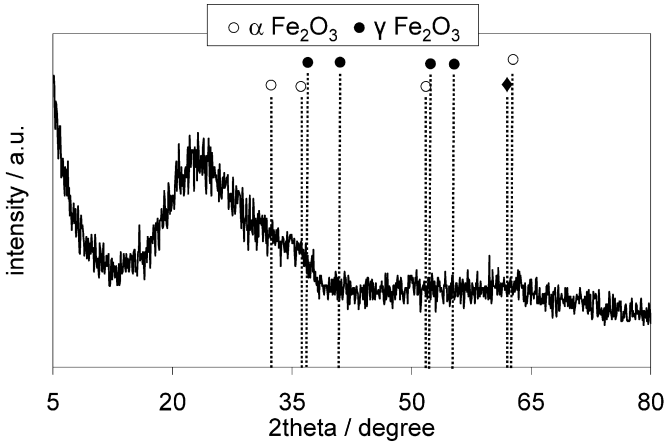

Fig. 3. XRD pattern of the calcined Fe17/SIM catalyst.

SIM surface in both the cases; denser iron phase could be observed on Fe17/SIM than on Fe6/SIM, but any large iron aggregates cannot be individuated.

All the calcined Fe-samples showed amorphous patterns and any peaks were not observed in any case, no matter the Fe oxide concentration (Fig. 3). The question that arises about the Fe_2O_3 phase is if it is present as a true amorphous phase or as small nanocrystalline particles below the detection size limit of the XRD [71]. It is known that nanoparticles of amorphous Fe_2O_3 crystallize into nanocrystalline maghemite γ-F_2O_3 [72], while for the Fe_2O_3–SiO_2 amorphous nanoparticles, the same transformation is shifted at higher temperature (i.e. 700 °C). The observed shift is the consequent stabilization of the amorphous Fe_2O_3 nanophase to what is called the preventive role of the silica matrix [72]. However, because our samples were calcined at 500 °C and because the absence of any line broadening at any characteristic 2θ position for crystallite Fe_2O_3 phases, even for the samples with the highest

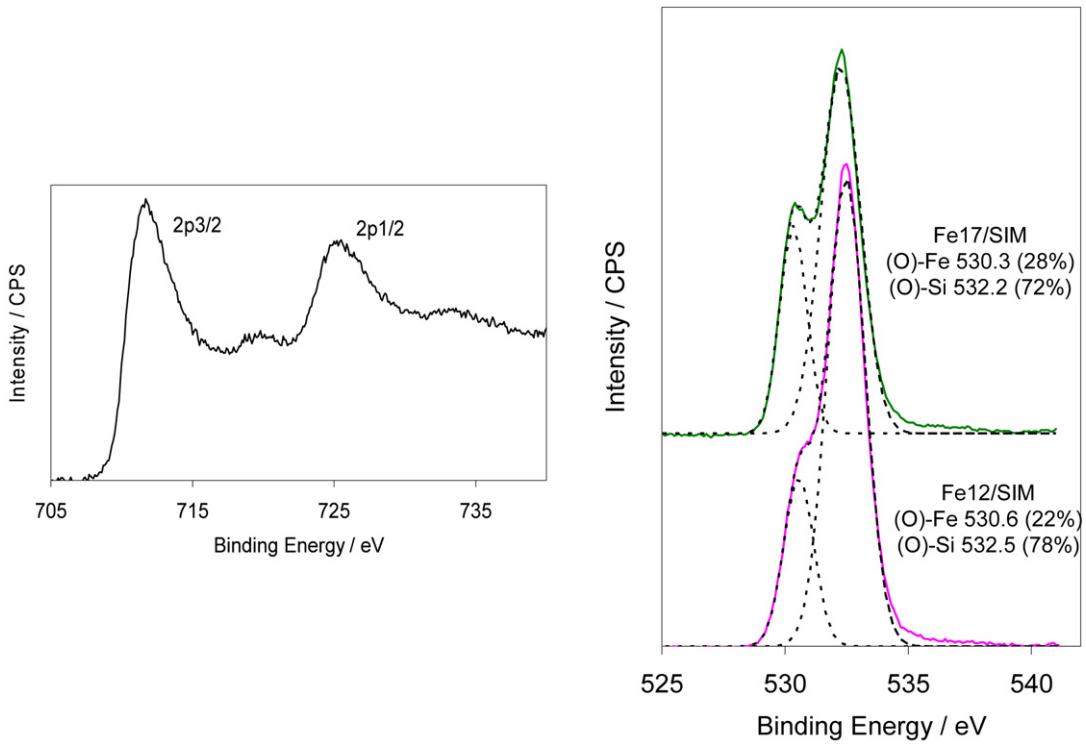

Fig. 4. XP spectrum of the Fe 2p region of a representative Fe-catalyst (Fe12/SIM) (left); O 1s XPS band for two selected Fe catalysts with band deconvolution (right): peak component typical of SiO_2, (O)–Si, at ca. 532 eV, and of Fe_2O_3, (O)–Fe, at ca. 530 eV. The surface concentrations of SiO_2 and Fe_2O_3 were calculated from the quantitative determination of the two oxygen peak components and indicated in the figure.

concentrations of iron, presence of amorphous Fe_2O_3 could invoke. Similar conclusions were reported by Khalil et al. [27] for their Fe_2O_3–SiO_2 nanocomposite materials.

The morphologic properties of SIM were completely changed by the iron deposition. The N_2-isotherms of adsorption–desorption of Fe-samples show that the height of the capillary condensation step decreases, the p/p_0 coordinate of the inflection point increases, and hysteresis appears (Fig. 1 shows the N_2-isotherms for Fe6/SIM, as an example). A very lower N_2-uptake is observed on the Fe-samples than on SIM, accounting for a decrease of the specific surface area and pore volume. As concerning the pore distribution of the Fe-samples, a very broad band centered at ca. 4 nm appeared shifted at larger pore size than SIM. This behavior suggests some extent of pore blocking of SIM by the deposited Fe oxo species. On the contrary, the decrease of the extension of surface area and porosity within the series of Fe-catalysts (from Fe4/SIM to Fe17/SIM) was restrained and regularly follows a decreasing exponential trend (Table 2). The observed decreasing can be explained by the progressive coverage of the SIM surface by the Fe oxide phase, possessing more reduced surface area and smaller porosity than silica.

Surface analysis by XPS confirmed the unique presence of Fe^{3+} in Fe_2O_3 environment on the basis of Fe 2p peak position and energy difference between the Fe($2p_{1/2}$) excited state and Fe($2p_{3/2}$) ground state [23,25,73–75]. All the catalyst surfaces had very similar positions for the Fe 2p values: Fe($2p_{3/2}$) peak at 711.5 ± 0.25 eV and Fe($2p_{1/2}$) peak at 725.0 ± 0.30 eV; the energy difference between the Fe($2p_{3/2}$) and Fe($2p_{1/2}$) being of 13.5 eV. In Fig. 4 (left side), it is reported the Fe(2p) core level of Fe12/SIM, chosen as an example. The O(1s) region can be deconvoluted into two peaks: 530.5 eV, corresponding to the oxygen within Fe_2O_3 [75], and 532.4 eV corresponding to the oxygen within the SiO_2 [26], which largely predominated (Fig. 4, right side). The (O)–Fe component of O(1s) band clearly increased passing from Fe12/SIM to Fe17/SIM indicating the effective surface enrichment of the iron oxide phase with the Fe loading. Concerning the nature of the iron species at the surface, the presence of FeO_x could be confirmed by calculating the atomic ratios of O–(Fe) (ca. 530 eV) to Fe 2p. The ratios were all around 1.33 (± 0.2), close but smaller that the expected 1.5 value, typical of Fe_2O_3. Likely, the totality of iron was not present as Fe_2O_3 but Fe-oxo species with lower oxygen coordination could be present. Concerning the surface Fe-concentration, the ratios determined by XPS ($Fe_{2p}/(Fe_{2p} + Si_{1s})$) and those calculated from the composition (Table 2) (Fe/(Fe + Si)) were comparable, in any case. This indicated that the totality of iron deposited on SIM was available at the surface, thus confirming the high Fe-dispersion for all the catalysts, independently of the Fe-concentration.

The dispersion and distribution of the iron species on the catalyst surfaces were elucidated by UV–DRS investigation. For all the samples, the UV–vis spectra show strong absorption with convoluted bands in a wavelength interval from 210 to 500 nm (Fig. 5). Each experimental curve could be deconvoluted into three subcurves with maxima (λ_{max}) at around 230, 360, and 500 nm. When changes of the extinction coefficients over the investigated wavelength range are neglected and contribution of the silica band in the same wavelength region can be neglected as well, because the very lower intensity, quantitative interpretation of the UV–vis bands could be tentatively assessed [76]. The spectra were dominated by the intense ligand to metal charge-transfer bands (LMCT bands, with intensities ranging from 55 to 65%) at high frequency (λ_{max} at 230 nm) that involve isolated 4-coordinated Fe^{3+} in $[FeO_4]^-$ tetrahedral ($t_1 \rightarrow t_2$ and $t_1 \rightarrow e$ transitions) [16,21,23,26,30,77,78]. The other absorption bands at lower frequencies (λ_{max} at 360 and 500 nm) were of very lower intensity, meaning that iron oligomers (low nuclearity $2d$-FeO_x species or ferric species ($3d$-Fe_2O_3) nanoparticles [16,21,23,26,30,76,77]) were not the prevalent species, even in the samples with high Fe-concentrations. Comparing the shape of all the UV–vis–DRS spectra of Fig. 5, it can be noted a red-shift of the spectra with increasing Fe concentration (from Fe4/SIM to Fe17/SIM). The observed

shift was almost exclusively due to the growing of the sub-curve centered at 360 nm, rather than that centered at 500 nm, that maintained a quite constant intensity (from 8 to 12%), independently of the Fe-concentration. The percent area of the bands at

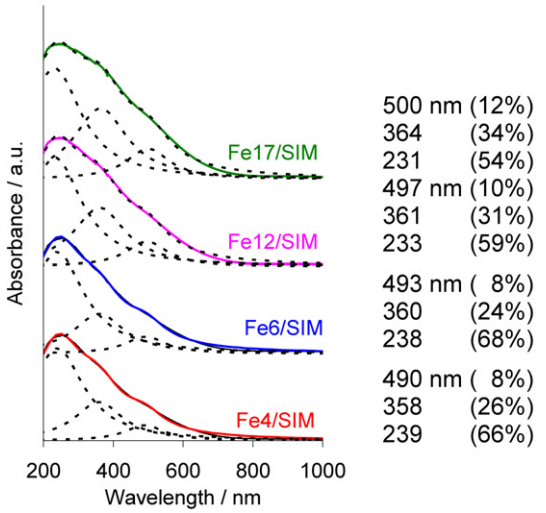

Fig. 5. UV–vis–DRS spectra of the Fe catalysts with curve deconvolution (maximum absorption wavelength and percentage area of each absorption are indicated for each sample).

λ_{max} at 360 nm was 26, 24, 31, and 34% for Fe4/SIM, Fe6/SIM, Fe12/SIM, and Fe17/SIM, respectively. Similarly, the ratio of the intensities of the band at 360 nm to that at 230 nm increased. Hence, the concentration of the species associated with the band at 360 nm ($2d$-FeO_x species) increased with Fe content in the sample. The observed Fe-clustering maintained always very moderate and it was smaller than that expected on the basis of the high Fe concentration of the most loaded Fe-samples.

The EPR spectra of the Fe-samples, recorded at r.t. and at −196 °C, are reported in Fig. 6. At both temperatures the spectra are similar, in particular those of Fe6/SIM, Fe12/SIM, and Fe17/SIM are almost identical. The spectra essentially consist of (i) a strongly temperature dependent signal at about 160 mT ($g \sim 4.3$) and (ii) a broad, rather featureless signal centered at about 320 mT ($g \sim 2.2$), spanning about 800 mT and featuring a broad peak-like feature at about 200 mT. These two signals are typical of Fe(III) within or on the surface of a siliceous material. The signal at $g \sim 4.3$ is due to isolated Fe(III) ions in a distorted tetrahedral coordination and its strong temperature dependence is dictated by Curie's law [79].

The broad spectral component is due to the presence of oligomeric iron oxide aggregates. To investigate the size distribution of these aggregates, we attempted to fit the experimental spectra to a model that already proved successful [26,80–82]. The model assumes that the Fe(III) species are iron oxide nanoparticles which exhibit a superparamagnetic behavior. Such behavior is characterized by a blocking temperature T_B, proportional to the

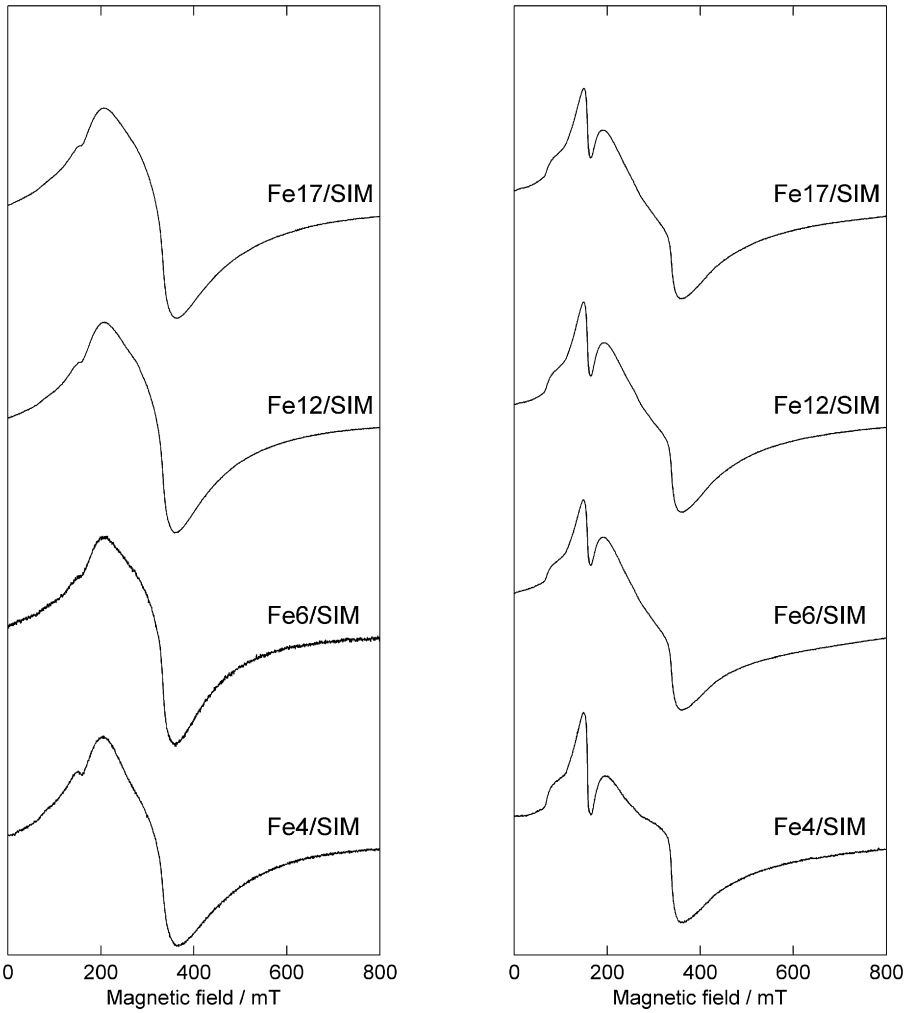

Fig. 6. EPR spectra of Fe-samples recorded at room temperature (left) and at −196 °C (right). The spectra are dominated by the broad component centered at about 320 mT. The composite feature centered at about 160 mT, which is due to isolated Fe(III) ions, is much larger in the low temperature spectra.

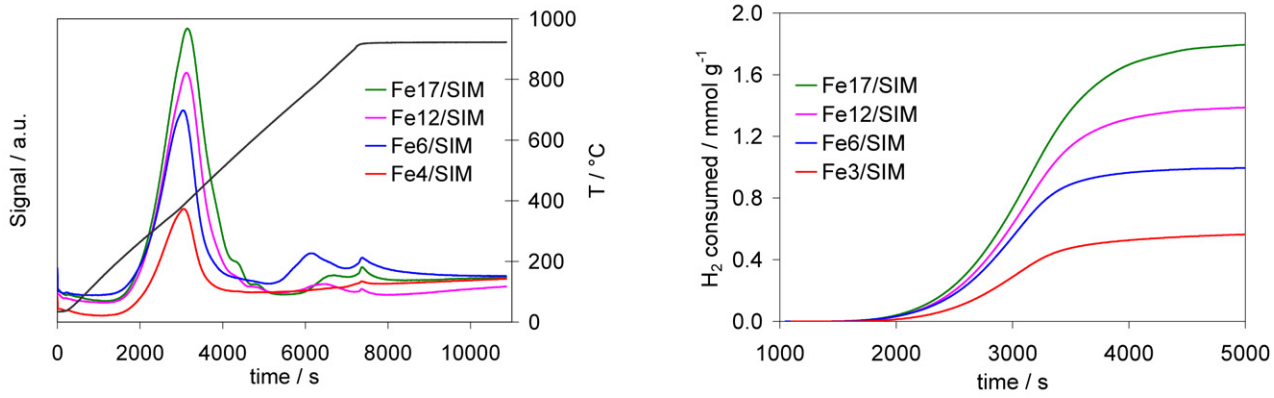

Fig. 7. Reduction profiles of the Fe-catalysts under TPR conditions (left) and specific H_2 consumptions (right) vs. analysis time/temperature.

Table 3
Results of reduction measurements by TPR analysis.

Sample	T_{max} (°C)	H_2 uptake (mmol g^{-1})		Reducing paths[a] (%)		
		Calculated[b]	Experimental	$Fe_2O_3 \rightarrow FeO$	$Fe_2O_3 \rightarrow Fe$	$Fe^{3+} \rightarrow Fe^{2+}$[c]
Fe4/SIM	392	0.771	0.586 (−24%)[d]	–	70	30
Fe6/SIM	393	1.262	0.932 (−26%)	–	69	31
Fe12/SIM	404	2.417	1.395 (−42%)	2	64	34
Fe17/SIM	407	3.223	1.793 (−44%)	8	60	32

[a] Percent hydrogen consumed from the three paths.
[b] Calculated assuming that all the iron phase present as Fe_2O_3 was reduced to Fe(0).
[c] Path leading to formation of fayalite phase.
[d] Percent variance of the experimental H_2 consumption relative to that calculated.

nanoparticle volume. At temperatures lower than T_B, the nanoparticles are in a blocked state and feature a very broad, anisotropic EPR spectrum. At temperatures higher than T_B, the nanoparticles behave as a superparamagnet and the EPR spectrum becomes narrower and less anisotropic. The observed EPR spectrum is the superposition of the spectra from nanoparticles with different volume and T_B. By fitting the observed spectra to this model, one obtains the size distribution of the iron oxide nanoparticles. Despite extensive attempts and some model refinement an unique size distribution that reproduced the experimental spectrum at a given temperature could not be found. Besides, the temperature dependence of the EPR spectrum could also not be reproduced.

Despite the failure of the superparamagnetic nanoparticle model to reproduce the broad EPR signal, we can however derive the following conclusions. The close similarity of the EPR spectra of all four Fe-samples suggests that the nature and relative fraction of the various Fe(III) species does not significantly depend on the total iron loading on the SIM support. In addition to the isolated, oxygen-coordinated Fe(III) ions, the Fe-samples contain iron oxide aggregates ranging in size from few nanometers to several tens of nanometers. The fraction of isolated Fe ions and Fe oxide aggregates cannot be quantitatively deduced from the EPR spectra. The qualitative deductions from the EPR results are in agreement with those from the UV–vis–DRS results.

By TPR analysis, not only the reducing properties of the supported iron oxide phase but also the dispersion and aggregation state could be disclosed [83,84]. TPR profiles of all the catalysts are shown in Fig. 7, which reports the results both as rate of H_2 consumption and integral H_2 consumption as a function of time/temperature of analysis. Blank TPR test on the bare support showed the inability of silica to consume hydrogen in the whole temperature range investigated. From a qualitative point of view, all the reducing profiles presented the same feature (Fig. 7): a main reduction peak with a well defined maximum at ca. 400 °C dominated the spectra, other weakly resolved maxima with very lower intensity at ca. 750 and 850 °C could be identified. The samples at progressively higher Fe loading consumed increasing amount of H_2 without any important modification of the shape and position of the reducing peaks.

The TPR profiles of the supported iron oxide samples appeared different from most of catalysts containing Fe oxide phases presented in the literature [26,85–88] that have two main reducing peaks in a wide temperature interval; the low-temperature peak is ascribed to hematite to wüstite reduction (Fe_2O_3 to FeO), with the possibility to identify the very easy Fe_2O_3 to Fe_3O_4 reducing step, the second peak to wüstite to zerovalent iron (FeO to Fe^0) reduction step (see Fig. 1S of Supporting Information). The difference between the present TPR profiles and those reported in the literature suggested that different reducing paths were concerned. The experimental H_2-consumptions were lower (from 25 to 45%) than those that could be calculated assuming total reduction of the iron phase from Fe_2O_3 (Table 3). It is hard to think that, at higher temperatures than that attained during experiments (900 °C), some more H_2 consumption could occur. A better deduction is that the silica matrix acted a strong inhibiting effect on the complete reduction of the iron oxide. Powder-XRD spectra of the reduced samples were collected to identify the iron-phases formed (XRD spectrum of reduced Fe17/SIM is shown as an example in Fig. 8). Three different crystalline phases containing iron can be clearly detected: fayalite (Fe_2SiO_4), wüstite (FeO), and the expected metallic iron (Fe^0). It can then be gathered that hydrogen reduced the present iron oxide to three different final products associated with three reducing paths: (i) from Fe^{3+} (dispersed ions in oxide environment) to Fe^{2+} (with fayalite formation), (ii) from Fe_2O_3 to wüstite (FeO); and (iii) from Fe_2O_3 to Fe(0). The hydrogen consumed experimentally could be justified taking into account the (i)–(iii) reactions above mentioned. Once known the total amount of iron in the samples (Table 2) and the amount of the dispersed Fe^{3+} ions, from UV–vis–DRS (66, 68, 59, and 54% for Fe4/SIM, Fe6/SIM, Fe12/SIM, and Fe17/SIM, respectively), the extent of hydrogen consumption from the (i)–(iii) reduction paths can be easily computed (an example of the computation can be found in

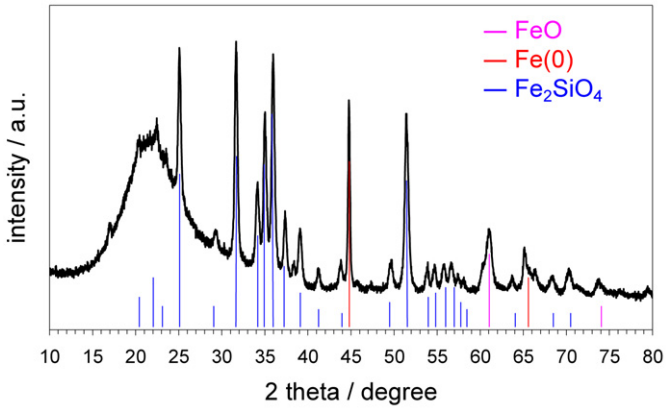

Fig. 8. XRD spectrum (step size 0.02° (2θ), time per step 10 s) of Fe17/SIM after TPR analysis.

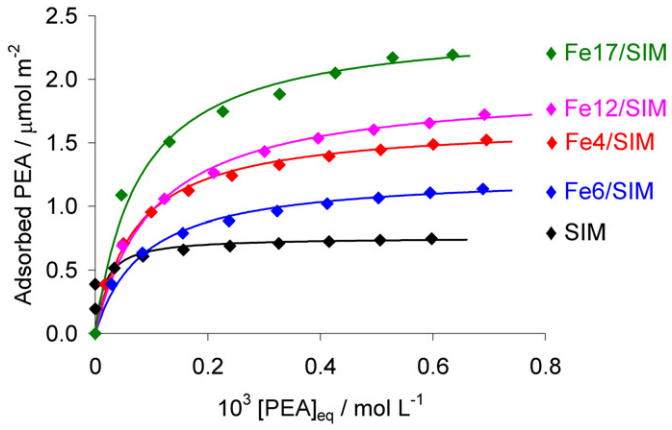

Fig. 9. Equilibrium isotherms of PEA adsorption at 17 °C in cyclohexane on the bare support and Fe-catalysts.

the Supporting Information). On all the samples, most of hydrogen was consumed to form metallic iron (Fe_2O_3 to Fe^0), this path decreased as higher the Fe-concentration, while reduction of Fe_2O_3 to FeO proceeded only in little extent on the most Fe concentrated samples. The remaining part of hydrogen was used to form the fayalite phase, by reduction of the Fe^{3+} ions dispersed on the silica surface (Table 3). The hydrogen consumed to form Fe_2SiO_4 was almost constant for all the samples, in agreement with UV–vis–DRS results that indicated the presence of Fe^{3+} isolated ions in a narrow amount in all the Fe-samples.

A peculiar feature of the Fe-samples was the acidity of the surfaces, for the presence of both the uncovered support surface (silanol groups) and supported iron phase. The titration of the SIM and Fe-samples by a strong base probe (2-phenylethylamine, PEA) showed that the Fe-deposition on SIM increased the total amount of surface acid sites with a well clear increasing trend for the samples with the highest Fe concentration (Fig. 9). The obtained PEA adsorption isotherms were numerically interpreted with the classical Langmuir model equation to obtain the number of acid sites (expressed as µequiv m^{-2}) and the Langmuir adsorption constant (b/M^{-1}). The obtained values are reported in Table 2 (see Table 1 for SIM). The average acid strength of the Fe-surfaces can be evaluated by the b adsorption constant values. The calculated b values were all comprised in a narrow interval (from 13,000 to 19,000 M^{-1}) without any clear increasing or decreasing trend with Fe-loading. This indicated that the supported iron oxide phases had no marked differences of acidity strength with Fe-concentration.

Table 4
Activity parameters of the Fe-catalysts in the α-pinene oxide (POX) isomerization.[a]

Sample	POX conversion[b] (%)	Selectivity[b] (%)				r°_{CPA}[c] (mmol (g_{cat} min)$^{-1}$)
		(CPA)	(PCP)	(TCV)	(TSB)	
Fe4/SIM	64.7	53.5	2.3	10.1	7.8	0.052
Fe6/SIM	74.9	51.4	2.4	10.8	6.9	0.047
Fe12/SIM	95.0	50.1	1.6	10.7	6.1	0.319
Fe17/SIM	100	52.8	1.2	11.3	6.0	0.384

[a] SIM attained ca. 20% POX conversion with an initial rate to CPA of 0.001 mmol (g_{cat} min)$^{-1}$.
[b] Data determined at 25 min of reaction. Campholenic aldehyde (CPA), pinocamphone (PCP), *trans*-carveol (TCV), and *trans*-sobrerol (TSB).
[c] Initial rate of α-campholenic aldehyde (CPA) formation.

An important question that the titration of the acid sites cannot solve is about the nature of the acid sites. To investigate on this important point, we measured the acid active sites in a catalytic test reaction (isomerization of α-pinene oxide), able to determine the presence of Brönsted rather than Lewis acid sites from the obtained product distribution.

3.2. Catalytic reaction

The catalytic acid-isomerization of POX can result in a large variety of products because of the high substrate reactivity [89]. Among the observed products, campholenic aldehyde (CPA), *trans*-carveol (TCV), *trans*-sobrerol (TSB), pinocamphone (PCP), and *para*-cymene (CIM) are the principal reaction products. CPA can only be prepared in high yield by using a suitable Lewis acid, PCP being the main byproduct. Brönsted acids tend to produce also TCV, CIM, TSB and dimerization products, so lowering the selectivity to CPA. Monitoring the product distribution during acid catalyzed α-pinene oxide isomerization is thus become a test for the Lewis acidity of a solid catalyst [58,89–92].

As a general trend over all the Fe-catalysts, quick conversion of α-pinene oxide (POX) was observed during the first 10–20 min, depending on the iron concentration in the sample, and then the reaction proceeded at lower rate, according with a first order kinetics. On all the Fe-catalysts, the reaction proceeded up to complete POX conversion that was attained in a time interval ranging from 25 min, for the sample containing the highest Fe concentration (Fe17/SIM), to 150 min for that with the lowest Fe-concentration (Fe4/SIM). Bare silica sample (SIM) showed a very low isomerization activity; after more than 1000 min only 45% POX conversion was attained.

In order to have comparative results among the different Fe-samples, the activity results have been compared at fixed reaction time of 25 min, correspondent to complete POX conversion of the catalyst with the highest iron concentration (Table 4). POX conversion regularly increased with Fe-concentration in the sample, while product distribution was very lightly affected by the Fe-loading. The main reaction products were campholenic aldehyde (CPA), pinocamphone (PCP), *trans*-carveol (TCV), and *trans*-sobrerol (TSB). These compounds took into account of more than 70% of all reaction products observed and they are the most significant in order to understand the acidic character of the catalytic sites. Some other products were present at lower percentage but they have not been included in the discussion. Campholenic aldehyde was the main reaction product with selectivity around 52–54% on all the catalysts, regardless of the Fe-content in the sample. *trans*-Carveol was detected in minor amount (around 11%) on all catalysts, and in decreasing amounts the *trans*-sobrerol (6–8%) and pinocamphone (1.5–2.5%) compounds were formed. Very similar product distributions, as that reported in Table 4, could be determined by evaluating the products at total POX conversion for all the catalysts. The

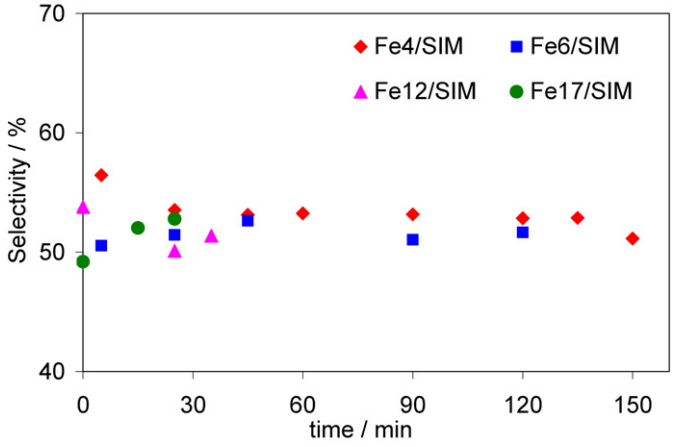

Fig. 10. Selectivity to α-campholenic aldehyde formed in the isomerization of α-pinene oxide vs. reaction time over all the Fe-catalysts.

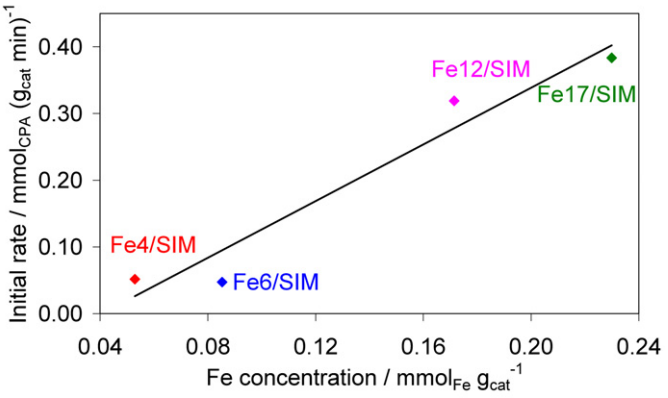

Fig. 11. Initial rate of α-campholenic aldehyde (CPA) formation as a function of the Fe concentration in each catalyst.

expected behavior reflects the fact that the products derive from a network of parallel reactions and the selectivity to reaction products is independent on the level of conversion. The trend of selectivity to CPA as a function of reaction time on all the Fe-catalysts is depicted in Fig. 10. It is clear that, not only selectivity to CPA did not change with reaction time (i.e., with POX conversion) for each catalyst, as above discussed, but any significant variation of its value was not observed among the different catalysts. This constant selectivity distribution obtained on all the samples suggested a constant distribution of the Fe-active sites on all the surfaces, in particular, isolated Fe sites and oligomeric Fe species (Table 4). The slight decrease of CPA selectivity with POX conversion observed in the first part of the reaction on some catalysts can be explained considering a selective poisoning of the strongest Lewis sites which rearranged the substrate to campholenic aldehyde.

The non-negligible presence of isomerization products typical of Brönsted acid sites transformation (TCV and TSB) could suggest a bifunctional acid character of the catalysts. Because of the presence of Fe^{3+} centers, acting as strong Lewis acid sites, the vicinal silanol groups of the silica support may become more acid than their intrinsic nature (SIM has quite silent catalytic ability), thus acquiring the catalytic ability of POX isomerizing. The sum of TCV and TSB obtained products was around 18% for all the Fe-catalysts, independently of Fe loading.

Aimed at collecting information on the activity of the active Lewis acid sites and in lack of the knowledge of the amount of active sites, the initial rates of POX conversion to CPA (r°_{CPA}) was calculated as explained in Section 2.3 and reported in Table 4. When the r°_{CPA} values were plotted against the Fe-concentration of each catalyst, linear trend could be identified. This trend indicated that new Fe active sites were continuously added on the surface after each iron loading on silica (see Scheme 1) without any significant modification of nature of the Fe species. Thus, the observed activity increase with Fe concentration (Fig. 11) led to a regular increase of yield to CPA (from 35% on Fe4/SIM to 53% on Fe17/SIM) without penalize selectivity to CPA.

4. Concluding remarks

In summary, highly dispersed Fe oxide supported catalysts on mesoporous silica with high Fe content were successfully synthesized by the equilibrium-adsorption route. The possibility to obtain such high Fe-loading and at the same time good dispersion of the small Fe oxo centers can be attributable to the characteristic of the silica that offered high amount of highly reactive silanol groups, in comparison with conventional silicas.

The results on Fe-*speciation*, electronic, redox, and acidic properties of the studied samples obtained from the various complementary physico-chemical investigations converged on the final deduction that by increasing of Fe-loading on the silica, even more Fe-sites were created without any important growing of the Fe-aggregates on the surface. The deposited iron phase on SIM was predominantly present as isolated Fe^{3+} ions and low nuclearity Fe oxo entities on all the catalyst surfaces, irrespective of Fe content. The catalytic activity of such Fe-sites was typical of Lewis acidity, as proved by the product distribution measured in the test reaction of α-pinene oxide isomerization. From this study emerged that the control of *speciation* on increasingly loaded Fe-catalysts can help in clarify the evolution of mono-, bi- and oligonuclear Fe-sites, with particular attention to the role of support in the stabilization of Fe-species.

Acknowledgments

This work has been partially supported by the Italian Research Ministry (FIRST project 2007). Authors would like to thank Professor Francesco Demartin (Dipartimento di Chimica Strutturale e Stereochimica Inorganica of the Università degli Studi di Milano) for his assistance in the XRD interpretation.

Supporting information

The online version of this article contains additional supporting information.

Please visit DOI: 10.1016/j.jcat.2008.12.016.

References

[1] A. Corma, H. Garcia, Chem. Rev. 103 (2003) 4307.
[2] A. Corma, Chem. Rev. 95 (1995) 559.
[3] G.A. Olah, Friedel–Crafts and Related Reactions, Wiley–Interscience, New York, 1963.
[4] G.A. Olah, Friedel–Crafts Chemistry, Wiley–Interscience, New York, 1973.
[5] I. Iovel, K. Mertins, J. Kischel, A. Zapf, M. Beller, Angew. Chem. Int. Ed. 44 (2005) 3913.
[6] G. Busca, Chem. Rev. 107 (2007) 5366.
[7] G. Sartori, R. Maggi, Chem. Rev. 106 (2006) 1077.
[8] Y. Sun, S. Walspurger, J.-P. Tessonier, B. Louis, J. Sommer, Appl. Catal. 300 (2006) 1.
[9] N. He, S. Bao, Q. Xu, Appl. Catal. A 169 (1998) 29.
[10] B.L. Cushing, V.L. Kolesnichenko, C.J. O'Connor, Chem. Rev. 104 (2004) 3893.
[11] J.B. Miller, E.I. Ko, Catal. Today 35 (1997) 269.
[12] D.R. Ulrich, CHEMTECH (1988) 242.
[13] J. Livage, Catal. Today 41 (1998) 3.
[14] K.M.S. Khalil, S.A. Makhlouf, Appl. Surf. Sci. 254 (2008) 3767.
[15] Q. Zhang, Q. Guo, X. Wang, T. Shishido, Y. Wang, J. Catal. 239 (2006) 105.
[16] Y. Li, Z. Feng, Y. Lian, K. Sun, L. Zhang, G. Jia, Q. Yang, C. Li, Micropor. Mesopor. Mater. 84 (2005) 41.

[17] Y. Li, Z. Feng, H. Xin, F. Fan, J. Zhang, P.C.M.M. Magusin, E.J.M. Hensen, R.A. van Santen, Q. Yang, C. Li, J. Phys. Chem. B 110 (2006) 26114.
[18] L. Peleanu, M. Zaharescu, I. Rau, M. Crisan, A. Jitianu, A. Meghea, J. Radioanal. Nucl. Chem. 246 (2000) 557.
[19] S. Lomnicki, B. Dellinger, Environ. Sci. Technol. 37 (2003) 4254.
[20] K. Bachari, J.M.M. Millet, P. Bonville, O. Cherifi, F. Figueras, J. Catal. 249 (2007) 52.
[21] K. Sun, H. Xia, Z. Feng, R. van Santen, E. Hensen, C. Li, J. Catal. 254 (2008) 383.
[22] M.J. Rokosz, A.V. Kucherov, H.-W. Jen, M. Shelef, Catal. Today 36 (1997) 65.
[23] T. Herranz, S. Rojas, F.J. Pérez-Alonso, M. Ojeda, P. Terreros, J.L.G. Fierro, Appl. Catal. A 308 (2006) 19.
[24] J.D. Henao, B. Wen, W.M.H. Sachtler, J. Phys. Chem. B 109 (2005) 2055.
[25] R.S. Prakasham, G.S. Devi, K.R. Laxmi, Ch.S. Rao, J. Phys. Chem. C 111 (2007) 3842.
[26] A. Gervasini, C. Messi, A. Ponti, S. Cenedese, N. Ravasio, J. Phys. Chem. C 112 (2008) 4635.
[27] K.M.S. Khalil, H.A. Mahmoud, T.T. Ali, Langmuir 24 (2008) 1037.
[28] J.A. Schwarz, C. Contescu, A. Contescu, Chem. Rev. 95 (1995) 477.
[29] K. Bourikas, C. Kordulis, A. Lycourghiotis, Catal. Rev. Sci. Eng. 48 (2006) 363.
[30] F. Arena, G. Gatti, G. Martra, S. Coluccia, L. Stievano, L. Spadaro, P. Famulari, A. Parmaliana, J. Catal. 231 (2005) 365.
[31] A. Gervasini, P. Carniti, S. Bennici, C. Messi, Chem. Mater. 19 (2007) 1319.
[32] S. Bennici, A. Auroux, C. Guimon, A. Gervasini, Chem. Mater. 18 (2006) 3641.
[33] S. Bennici, P. Carniti, A. Gervasini, Catal. Lett. 98 (2004) 187.
[34] J.S. Beck, J.C. Vartuli, W.J. Roth, M.E. Leonowicz, C.T. Kresge, K.D. Schmitt, C.T.W. Chu, D.H. Olson, E.W. Sheppard, S.S.B. McCullen, J.B. Higgins, J.L. Schlenker, J. Am. Chem. Soc. 114 (1992) 10834.
[35] C.T. Kresge, M.E. Leonowicz, W.J. Roth, J.C. Vartuli, J.S. Beck, Nature 359 (1992) 710.
[36] D. Zhao, J. Feng, Q. Huo, N. Melosh, G.H. Fredrickson, B.F. Chmelka, G.D. Stucky, Science (Washington, DC) 279 (1998) 548.
[37] S.A. Bagshaw, E. Prouzet, T.J. Pinnavaia, Science (Washington, DC) 269 (1995) 1242.
[38] R. Ryoo, J.M. Kim, C.H. Ko, C.H. Shin, J. Phys. Chem. 100 (1996) 17718.
[39] S. Inagaki, A. Koiwai, N. Suzuki, Y. Fukushima, K. Kuroda, Bull. Chem. Soc. Jpn. 69 (1996) 1449.
[40] Y. Wan, Y. Shi, D. Zhao, Chem. Commun. (2007) 897.
[41] R. Zhang, P. Somasundaran, Adv. Colloid Interface Sci. 123–126 (2006) 213.
[42] G.J. de A.A. Soler-Illia, C. Sanchez, B. Lebeau, J. Patarin, Chem. Rev. 102 (2002) 4093.
[43] A. Corma, Chem. Rev. 97 (1997) 2373.
[44] J.Y. Ying, C.P. Mehnert, M.S. Wong, Angew. Chem. Int. Ed. 38 (1999) 56.
[45] A. Sayari, Chem. Mater. 8 (1996) 1840.
[46] K. Moller, T. Bein, Chem. Mater. 19 (1998) 2950.
[47] A. Sayari, Chem. Mater. 8 (1996) 1840.
[48] A.P. Wight, M.E. Davis, Chem. Rev. 102 (2002) 3589.
[49] D.E. De Vos, M. Dams, B.F. Sels, P.A. Jacobs, Chem. Rev. 102 (2002) 3615.
[50] T. Linssen, P. Cassiers, E.F. Vansant, Adv. Colloid Interface Sci. 103 (2003) 121.
[51] A. Stein, Adv. Mater. 15 (2003) 763.
[52] S. Dai, M.C. Burleigh, Y. Shin, C.C. Morrow, C.E. Barnes, Z. Xue, Angew. Chem. Int. Ed. 38 (1999) 1235.
[53] Y. Lin, G.E. Fryxell, H. Wu, M. Engelhard, Environ. Sci. Technol. 35 (2001) 3962.
[54] C.-Y. Lai, B.G. Trewyn, D.M. Jeftinija, K. Jeftinija, S. Xu, S. Jeftinija, V.S.Y. Lin, J. Am. Chem. Soc. 125 (2003) 4451.
[55] V.S. Lin, C.-Y. Lai, J. Huang, S.-A. Song, S. Xu, J. Am. Chem. Soc. 123 (2001) 11510.
[56] S. Huh, J.W. Wiench, J.-C. Yoo, M. Pruski, V.S.-Y. Lin, Chem. Mater. 15 (2003) 4247.
[57] N. Ravasio, F. Zaccheria, M. Guidotti, R. Psaro, Top. Catal. 27 (2004) 157.
[58] N. Ravasio, F. Zaccheria, A. Gervasini, C. Messi, Catal. Commun. 9 (2008) 1125.
[59] E.P. Barrett, L.G. Joyner, P. Halenda, J. Am. Chem. Soc. 73 (1951) 373.
[60] P. Malet, A. Caballero, J. Chem. Soc. Faraday Trans. 1 84 (1988) 2369.
[61] D.A.M. Monti, A. Baiker, J. Catal. 83 (1983) 323.
[62] P. Carniti, A. Gervasini, S. Biella, Adsorp. Sci. Technol. 23 (2005) 739.
[63] L. Fu, R.A. Sá Fereira, A. Valente, J. Rocha, L.D. Carlos, Micropor. Mesopor. Mater. 94 (2006) 185.
[64] C. Perego, S. Amarilli, A. Carati, C. Flego, G. Pazzuconi, C. Rizzo, G. Bellussi, Micropor. Mesopor. Mater. 27 (1999) 345.
[65] S. Ek, A. Root, M. Peussa, L. Niinistö, Thermochim. Acta 379 (2001) 201.
[66] J. Mrowiec-Bialoń, Thermochim. Acta 443 (2006) 49.
[67] R. Mueller, H.K. Kammler, K. Wegner, S.E. Pratsinis, Langmuir 19 (2003) 160.
[68] C.G. Armistead, A.J. Tyler, F.H. Hambleton, S.A. Mitchell, J.A. Hockey, J. Phys. Chem. 73 (1969) 3947.
[69] J.J. Fripiat, J. Uytterhoeven, J. Phys. Chem. 66 (1965) 800.
[70] H.E. Ries, K.J. Laidler, W.E. Innes, F.G. Ciapetta, C.J. Plank, P.W. Selwood, in: P.H. Emmett (Ed.), Catalysis, vol. I, Fundamental Principles (Part I), Book Division Reinhold Publishing Corporation, New York, 1954, p. 258.
[71] L. Machala, R. Zboril, A. Gedanken, J. Phys. Chem. B 111 (2007) 4003.
[72] G. Ennas, A. Musinu, G. Piccalunga, D. Zedda, D. Gatteschi, C. Sangregorio, J.L. Stanger, G. Concas, G. Spano, Chem. Mater. 10 (1998) 495.
[73] J.D. Walker, R. Tannenbaum, Chem. Mater. 18 (2006) 4793.
[74] L. Dghoughi, B. Elidrissi, C. Bernède, M. Addou, M. Alaoui Lamrani, M. Regragui, H. Erguig, Appl. Surf. Sci. 253 (2006) 1823.
[75] Y. Joseph, G. Ketteler, C. Kuhrs, W. Ranke, W. Weiss, R. Schlögl, Phys. Chem. Chem. Phys. 3 (2001) 4141.
[76] M. Schwidder, S. Heikens, A. De Toni, S. Geisler, M. Berndt, A. Brückner, W. Grünert, J. Catal. 259 (2008) 96.
[77] S. Bordiga, R. Buzzoni, F. Geobaldo, C. Lamberti, E. Giamello, A. Zecchina, G. Leofanti, G. Petrini, G. Tozzola, G. Vlaic, J. Catal. 158 (1996) 486.
[78] A. Tuel, I. Arcon, J. Millet, J. Chem. Soc. Faraday Trans. 94 (1998) 3501.
[79] M. Ferretti, A.L. Barra, L. Forni, C. Oliva, A. Schweiger, A. Ponti, J. Phys. Chem. B 108 (2004) 1999, and references therein.
[80] J.L. Dormann, D. Fiorani, E. Tronc, Adv. Chem. Phys. 98 (1997) 283.
[81] R. Berger, J.C. Bissey, J. Kliava, B. Soulard, J. Magn. Magn. Mater. 167 (1997) 129.
[82] J. Kliava, R. Berger, J. Magn. Magn. Mater. 205 (1999) 328.
[83] C. Messi, P. Carniti, A. Gervasini, J. Therm. Anal. Cal. 91 (2008) 93.
[84] M. Fadoni, L. Lucarelli, Stud. Surf. Sci. Catal., vol. 120A (A. Dabrowski (Ed.), Adsorption and Its Applications in Industry and Environmental Protection, vol. 1), Elsevier, Amsterdam, 1999, pp. 177–225.
[85] K.D. Chen, Y.N. Fan, Z. Hu, Q.J. Yan, Catal. Lett. 36 (1996) 139.
[86] K. Chen, Q. Yan, Appl. Catal. A 158 (1997) 215.
[87] H. Hayashi, L.Z. Chen, T. Tago, M. Kishida, K. Wakabayashi, Appl. Catal. A 231 (2002) 81.
[88] T. Herranz, S. Rojas, F.J. Pérez-Alonso, M. Ojeda, P. Terreros, J.L.G. Fierro, Appl. Catal. A 308 (2006) 19.
[89] W.F. Holderich, J. Roseler, G. Heitmann, A.T. Liebens, Catal. Today 37 (1997) 353.
[90] J. Kaminska, M.A. Schwegler, A.J. Hoefnagel, H. van Bekkum, Recl. Trav. Chim. Pays-Bas 111 (1992) 432.
[91] L. Alaerts, E. Séguin, H. Poelman, F. Thibault-Starzyk, P.A. Jacobs, D.E. De Vos, Chem. Eur. J. 12 (2006) 7353.
[92] G. Neri, G. Rizzo, S. Galvagno, G. Loiacono, A. Donato, M.G. Musolino, R. Pietropaolo, E. Rombi, Appl. Catal. A 274 (2004) 243.